Contents lists available at ScienceDirect

Applied Catalysis B: Environmental

Strongly coupled CdS/graphene quantum dots nanohybrids for highly efficient photocatalytic hydrogen evolution: Unraveling the essential roles of graphene quantum dots

Yonggang Lei [a], Cheng Yang [a], Jianhua Hou [a], Fang Wang [a], Shixiong Min [a,*], Xiaohua Ma [a], Zhiliang Jin [a], Jing Xu [a], Gongxuan Lu [b], Kuo-Wei Huang [c]

[a] School of Chemistry and Chemical Engineering, Beifang University of Nationalities, Yinchuan 750021, Ningxia Province, China
[b] State Key Laboratory for Oxo Synthesis and Selective Oxidation, Lanzhou Institute of Chemical Physics, Chinese Academy of Sciences, Lanzhou 730000, China
[c] KAUST Catalysis Center, King Abdullah University of Science and Technology, Thuwal 23955-6900, Saudi Arabia

ARTICLE INFO

ABSTRACT

It have been recognized that the coupling of graphene quantum dots (GQDs) with semiconductor photocatalysts endow the resulting nanocomposites with enhanced photocatalytic performances, however, the essential roles of GQDs have not been clearly revealed yet. Herein, we report that a high efficiency of the photocatalytic H_2 evolution was achieved using strongly coupled nanohybrids of CdS with GQDs (CdS/GQDs) as visible-light-driven photocatalysts. CdS/GQDs nanohybrids were synthesized by a facile hydrothermal method in which the crystallization of CdS precursor and coupling of GQDs could be accomplished in one-step. GQDs are firmly decorated on the surface of CdS nanoparticles, forming "dot-on-particle" heterodimer structures. GQDs have no significant influence on the crystallite structure of CdS but render the nanohybrids with strong light absorption at the wavelength beyond the band edge of CdS. Under visible light irradiation ($\geq$420 nm), CdS/GQDs nanohybrids reach the highest H_2 production rate of 95.4 μmol·h^{-1}, about 2.7 times higher than that of pure CdS nanoparticles, at GQDs content of 1.0 wt%, and the apparent quantum efficiency (AQE) was determined to be 4.2% at 420 nm. Incident light-wavelength dependent experiments reveal that the light absorption of CdS dominated the performance of nanohybrids, and the excess light absorption coming from GQDs hardly contributes to the observed higher activity. Photocurrent response, steady-state and time-resolved PL, and EIS measurements suggest that the high activity of CdS/GQDs is attributed predominantly to the graphene-like nature of GQDs, which can act as an efficient electron acceptor to induce an efficient charge separation. This work clearly reveals that GQDs mainly played a role of electron acceptor instead of a photosensitizer in enhancing the photocatalytic H_2 evolution performances of CdS/GQDs nanohybrids, which offers a new insight to understand the essential roles of GQDs in semiconductor/GQDs nanohybrids for efficient solar energy conversion applications.

© 2017 Elsevier B.V. All rights reserved.

1. Introduction

Graphene quantum dots (GQDs) are composed of single- or few-layer graphene microdomains with a typical lateral size less than ~20 nm and represent a new type of zero-dimensional (0D) carbon nanomaterials with combined unique properties of graphene and quantum dots [1–3]. Specifically, owing to the size-resulted quantum confinement and strong edge effects, GQDs have exhibited unique optoelectronic properties [4–8], such as tunable bandgap, strong visible light absorption, excellent photostability, and biocompatibility. Equally important, GQDs also have excellent solution-processable feature because of their amphilicity in common solvents [2]. Therefore, as a result of extraordinary optoelectronic and surface chemistry properties of GQDs, a verity of important potential applications has been explored on the GQDs-based materials in bioimaging [9,10], biosensing [11,12], photodynamic therapy [13,14], catalysis [15–17], in particular energy-conversion-related fields [3,18]. Most recently, the application of GQDs has also been increasing exploited in photocatalytic and photoelectrochemical devices inspired by the past success

utilization of graphene for improving the performances of energy-conversion systems [19–45].

It has been reported that GQDs itself can be directly used as a metal-free photocatalyst for overall water splitting and dye degradation [19–22]. For example, Teng and coworkers [20,21] have reported that nitrogen-doped GQDs (NGO-QDs) were capable of photocatalytically splitting pure water into H_2 and O_2 under visible light (>420 nm). A Z-scheme electron transfer originated from coexistence of p- and n-type conductivity domains in NGO-QDs was proposed to account for the observed photocatalytic activity. In the following studies, GQDs were also used to functionalize the photoactive inorganic and organic materials (semiconductors (SCs)[23–36], polymers [39,40], and dyes [41–45]) for developing advanced nanohybrids with enhanced performances. Specifically, GQDs have been coupled with several SCs including UV-light-responsive TiO_2 and ZnO as well as visible-light-responsive CdSe for photo(electro)catalytic applications. It has been reported by Chan and Gupta et al. [25,26] that GQDs infilled/modified TiO_2 nanotube arrays (TNTs) exhibited higher activity for dye degradation under UV or visible light irradiation. Congruously, Pan et al. [27] have observed an enhanced separation efficiency of electron-hole pairs in GQDs by forming heterojunctions with TiO_2, and as a result an improved visible light activity for dye degradation (>420 nm) were achieved compared to their pure counterparts. Guo et al. [33] have showed that sensitization of ZnO nanowire arrays with GQDs resulted in an enhanced IPCE for photoelectrochemical water splitting in a PEC device for all wavelengths longer than 400 nm compared to ZnO NWs. Hus et al. [28] have reported an promoted H_2 production activity on CdSe nanocrystals by loading GQDs in PEC cell under light irradiation with longer wavelengths (460–550 nm). These results have pointed out that the GQDs most likely serve as a photosensitizer to enhance light absorption ability, and thus improving the catalytic performances. However, for above GQDs-based nanohybrids, the visible-light-activity was usually observed for dye degradation reactions [23–25,27], where a dye sensitization effect cannot be completely excluded for observed higher activity. On the other hand, as to the enhanced IPCE in PEC cells, although the excess photons absorbed by GQDs can be converted to electrons for producing electricity, this could not be the case in photocatalysis applications, where the photogenerated electrons on GQDs have not been confirmed to induce chemical reactions involved in dye degradation and H_2 evolution processes. Furthermore, in the development of polymer-based and dye-sensitized solar cells [39–42], the incorporation of GQDs can greatly enhance the IPCE of the devices, and the GQDs were identified as efficient electron transfer mediator to promote charge separation efficiency. Moreover, GQDs have also been used to construct visible-light-driven dye-sensitized photocatalytic H_2 evolution systems [43,44], where Pt as H_2 evolution cocatalyst was combined with GQDs. In these systems, the excited dye has much negative reduction potentials than LUMO energy level of GQDs, and thus the transfer of photogenerated electrons from dye to GQDs and then to Pt cocatalyst is thermodynamically favorable. However, the role of GQDs as electron acceptor is still obscure because the presence of GQDs can also act as support to improve the dispersion of Pt and thus enhancing the H_2 evolution activity of the studied systems [17].

Overall, although unexceptionally enhanced performances have been demonstrated due to the presence of GQDs, the essential roles of GQDs still need to be clearly revealed to identify the governing factor for controlling surface charge production, transfer, and separation as well as photocatalytic activity in GQDs-based nanohybrid materials. Cadmium sulfide (CdS), as a model visible-light-responsive semiconductor, has been extensively studied for applications in photocatalytic and photoelectrochemical water reduction because of its narrow band-gap (~2.4 eV) matched for maximizing visible light absorption of solar spectrum and excel-

lent photocatalytic activity for H_2 evolution [46–48]. However, the higher recombination rate of photogenerated electron-hole pairs and stability concerns raised by photocorrosion during the photocatalytic reactions still need to be addressed to ensure its practical applications. One of the most widely used strategies is to combine CdS with conductive carbon nanomaterials to effectively facilitate the transfer of the photogenerated electrons to the surface of photocatalysts and alleviate photocorrosion issues. So far, graphene, carbon nanotubes, and fullerene have been extensively used for realizing abovementioned merits [49–51]; however, to the best of our knowledge, there is no previous work studying the GQDs mediated electron transfer behaviors of CdS and the photocatalytic H_2 evolution activity of resulting composites. In the present study, we employed a facile hydrothermal method to prepare the nanohybrids of CdS nanoparticles and GQDs, where the GQDs were firmly decorated on the surface of CdS nanoparticles via a chemical interaction, forming strongly coupled CdS/GQDs nanohybrids. The morphologies, microstructures, optical properties, and in particular the interaction between two components were investigated in detail. The photocatalytic H_2 evolution activity of resulting CdS/GQDs nanohybrids were evaluated under visible light irradiation. The incident light wavelength-dependent activity, photoelectrochemical, steady-state and time-resolved PL measurements were used to clarify the role of GQDs in enhancing the photocatalytic performances of CdS/GQDs nanohybrids. On the basis of above results, a possible mechanism of the improved photocatalytic activity was also proposed.

2. Experimental

2.1. Chemicals and reagents

All reagents were of analytical grade and used without further purification. Pyrene was purchased from Sigma-Aldrich. Deionized (DI) water was produced using an YL-100B-D water purification system (resistivity > 15 MΩ).

2.2. Preparation of GQDs, CdS nanoparticles, and CdS/GQDs nanohybrids

2.2.1. Synthesis of GQDs [32,52]

2 g of pyrene was nitrated into 1,3,6-trinitropyrene (TNP) in hot HNO_3 (160 mL) at 80 °C under refluxing and stirring for 12 h [52]. After cooled to room temperature, the mixture was diluted with DI water (2 L) and filtered to remove the acid and washed with water for several times. 0.5 g of TNP was then dispersed into 40 mL of hydrazine hydrate solution (0.2 M) by ultrasonication (150 W, 40 kHz) for 5 h. Next, the suspension was transferred into a Teflon-lined autoclave (100 mL) and heated at 150 °C for 10 h. After cooled to room temperature, the product containing water-soluble GQDs was successively filtered through a 0.22 μm and a 25 nm microporous membrane to remove traces of insoluble impurities.

2.2.2. Synthesis of CdS nanoparticles

An aqueous solution of Na_2S (800 mL, 0.14 M) was added slowly to $Cd(CH_3COO)_2$ solution (1000 mL, 0.14 M) under vigorous stirring. The yellow mixture was stirred for 24 h and kept for an additional 24 h. The resulting yellow slurry was filtered, thoroughly washed with water, and dried at 40 °C for 24 h.

2.2.3. Synthesis of CdS/GQDs nanohybrids

The CdS/GQDs nanohybrids were prepared by a facile hydrothermal deposition method. Typically, 0.5 g of CdS nanoparticles was dispersed into 60 mL of DI water containing different amount of GQDs with ultrasonication and stirring for 1 h at room temperature to form a homogeneous suspension. The weight ratios

of GQDs to CdS were 0, 0.25%, 0.5%, 1.0%, 1.5%, 2.0%, and 3.0%, and the obtained samples were labeled as CG0, CG0.25, CG0.5, CG1.0, CG1.5, CG2.0, and CG3.0, respectively. After that, the suspension was transferred into a Teflon-lined autoclave (100 mL) and maintained at 180 °C for 6 h. After cooled to room temperature, the product was collected by filtration through a 0.22 μm microporous membrane, washed with water and ethanol for several times, and dried in air for overnight.

2.3. Characterizations

The crystalline structures of the samples were investigated with a Rigaku B/Max-RB diffractometer with a nickel filtrated Cu $K\alpha$ radiation operated at 40 kV and 40 mA. The morphologies of the samples were observed with a Tecnai-G2-F30 field emission transmission electron microscope. X-ray photoelectron spectroscopy (XPS) measurements of the samples were performed on a K-Alpha surface analysis (Thermon Scientific) using X-ray monochromatization. Fourier transform infrared spectroscopy (FT-IR) spectra were performed on Thermo Nicolet Avatar 380 FT-IR spectrometer. Raman spectra were recorded with a DXR2 Raman microscope (Thermo Scientific) with a 633 nm He-Ne laser as excitation source at room temperature. UV–vis diffuse reflectance spectra were recorded on a Shimadzu UV-3600 UV–vis-near-IR spectrophotometer equipped with an integrating sphere and BaSO$_4$ powders were used as a reflectance standard. UV–vis absorption spectra were obtained with a TU-1810 UV–vis spectrophotometer (Beijing Persee). Photoluminescence spectra were determined by a Horiba Scientific FluoroMax-4 spectrofluorometer spectrometer. The fluorescence decay times were measured using the Horiba Jobin Yvon Data Station HUB operating in time-correlated single photon counting mode (TCSPC) with the time resolution of 200 ps. Nano LED diode emitting pulses at 370 nm with 1 MHz repetition rate was used as an excitation source. Light-scattering Ludox solution was used to obtain the instrument response function (prompt). The time ranges are 0.055 ns/channel in 4096 effective channels.

2.4. Photocatalytic hydrogen evolution

The photocatalytic hydrogen production experiments were performed in a 250 mL Pyrex reaction cell connected to a closed gas circulation and evacuation system (CEL-SPH2N, CEAULIGHT). A 300-W Xe lamp (CEL-HXF300) equipped with an optical cut-off filter ($\lambda \geq 420$ nm) was used as light source. In a typical experiment, 40.0 mg of the photocatalyst was dispersed into 100 mL of aqueous solution containing 0.5 M Na$_2$S and 0.5 M Na$_2$SO$_3$ as the sacrificial reagents by ultrasonication for 5 min. Before irradiation, the reac-

tion system was thoroughly degassed by evacuation in order to remove the oxygen inside. The reaction solution was continuously stirred and maintained at 304 K by a flow of cooling anhydrous ethanol during the photocatalytic reaction. The amount of evolved H$_2$ was determined using an on-line gas chromatograph (CEL-GC-7920, TCD, N$_2$ carrier). The apparent quantum efficiency (AQE) was measured under the same photocatalytic reaction conditions with irradiation light through a band-pass filter of 420 nm. The photon flux of incident light was determined using a Ray virtual radiation actinometer (Apogee MQ-500, silicon ray detector, light spectrum, 389–692 nm; measurement range, 0–4000 μmol^{-1} m^{-2} s^{-1}). The AQE was calculated from the ratio of the number of reacted electrons during hydrogen evolution to the number of incident photons.

2.5. Photoelectrochemical measurements

Electrochemical and photoelectrochemical measurements were carried out in a three-electrode cell made of quartz using an electrochemical workstation (CHI660E, Shanghai, China). A Pt sheet and a saturated calomel electrode (SCE) were used as the counter and reference electrodes, respectively. The working electrodes of CG0 and CG1.0 were prepared by drop-casting 0.25 mL of CG0 and CG1.0 suspensions in water (8.0 mg·mL^{-1}) onto clean conductive areas of *ca. 1.0* cm × 1.5 cm of FTO glass. After that, the thin film electrodes were dried in flow air overnight and dried at 50 °C for additional 12 h. The effective irradiation areas of as-prepared CG0 and CG1.0 electrodes were controlled to be 1.0 × 1.0 cm². To ensure a certain stability of the photoanodes, a mixed solution containing 0.5 M Na$_2$SO$_3$ and 0.5 M Na$_2$S was used as supporting electrolyte and sacrificial reagent with N$_2$ bubbling (40 mL/min) for over 10 min before tests. A 250-W Xe lamp equipped with an ultraviolet cutoff filter of 420 nm was utilized as the visible light source. The integrated visible light intensity reached on electrode surface was determined to be 42 mW cm^{-2}. The transient photocurrent response was recorded at a bias of 0 or 0.5 V under chopped light irradiation. Electrochemical impedance spectroscopy (EIS) were carried out at a forward bias of 0.7 V with AC amplitude of 10 mV and a frequency range of 10 mHz to 100 kHz in the dark or light irradiation. The Mott-Schottky analysis was conducted from −1.6 to 0.1 V at a frequency of 1 kHz in a solution containing 0.5 M Na$_2$SO$_3$ and 0.5 M Na$_2$S at a step of 50 mV s^{-1}. Flat band potential and majority-charge carrier concentration were determined from the Mott–Schottky plots.
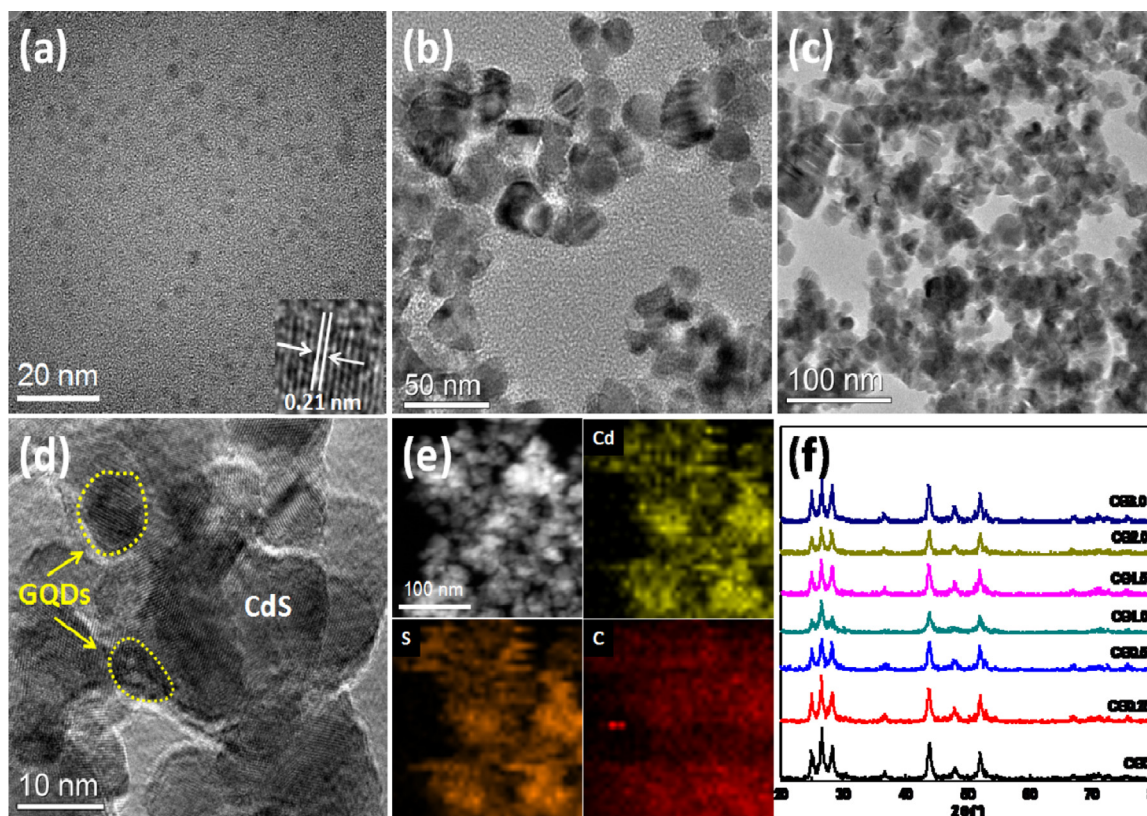
3. Results and discussion

Scheme 1 schematically illustrated the synthetic procedure of CdS/GQDs nanohybrids by a facile hydrothermal coupling of
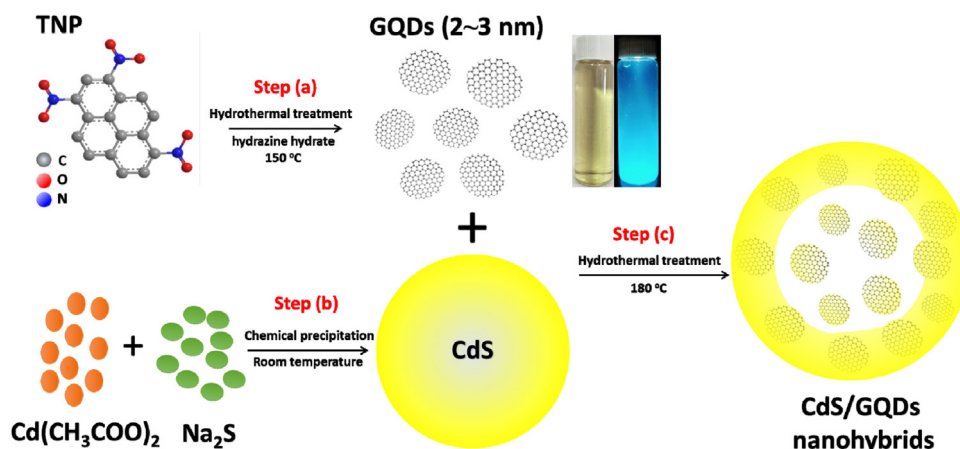
Scheme 1. Schematic illustration of the preparation process of graphene quantum dots (GQDs) (step (a)), CdS nanoparticles (step (b)), and CdS/GQDs nanohybrids (step (c)).

Fig. 1. TEM images of GQDs (a), pure CdS nanoparticles (b) (sample CG0), and CG1.0 sample (c). The inset in panel (c) shows the HRTEM image of individual GQD with a space of 0.21 nm lattice spacing for the graphene (100) planes. HRTEM image of sample CG1.0 (d) and corresponding HAADF-STEM image as well as Cd, S, and C elemental mappings (e). (f) The XRD patterns of the samples.

graphene quantum dots (GQDs) and CdS nanoparticles under mild conditions. Firstly, high-quality GQDs were prepared by a facile intramolecular fusion of 1,3,6-trinitropyrene (TNP) molecules catalyzed by hydrazine hydrate in aqueous solutions under mild hydrothermal conditions (step (a)) [32,52], whereas CdS nanoparticles were simply obtained by reacting $Cd(CH_3COO)_2$ with Na_2S in aqueous solutions at room temperatures (step (b)). The as-prepared GQDs were highly fluorescent and showed an excitation wavelength-independent emission feature (Fig. S1) [52]. The as-prepared CdS nanoparticles are in cubic crystal phase and have high surface areas ($96.4\,m^2\,g^{-1}$) but low crystallinity (Fig. S2). Secondly, the as-prepared GQDs and CdS were mixed into water and ultrasonically dispersed for 30 min, by which the GQDs can be homogeneously and steadily adsorbed on the surface of CdS nanoparticles. In the following hydrothermal treatment (step (c)), the cubic CdS were transformed to well-crystallized hexagonal CdS (*vide infra*) and the GQDs were stably immobilized on the surface of CdS nanoparticles to form strongly coupled CdS/GQDs nanohybrids [27–29].

Fig. 1a shows the TEM image of as-prepared GQDs, which reveals that the GQDs have a relatively uniform particle distribution, giving an average lateral size of ∼2.8 nm (Fig. S3). As displayed in its HRTEM image (inset in Fig. 1a), the individual GQDs are composed of defect-free graphene domains with a well-resolved interplanar spacing of ∼0.21 nm, corresponding to in-plane (100) facet of graphene [27,52]. The TEM image in Fig. 1b reveals that the pure CdS (sample CG0) consists of slightly aggregated nanoparticles with diameters of approximate 20–30 nm. After coupling CdS nanoparticles with GQDs under hydrothermal conditions, the TEM image (Fig. 1c) of resulting CdS/GQDs nanohybrids (sample CG1.0) shows that the incorporation of GQDs have no significant effect on the morphology and size of CdS nanoparticles but the distri-

bution of particles is lower compared to sample CG0, indicating that GQDs may react with CdS nanoparticles and thus induce the aggregation [28]. The HRTEM image of sample CG1.0 in Fig. 1d indicates that the nanohybrids appears as the "dot-on-particle" heterodimer structures with well-defined lattice fingers that can be respectively ascribed to GQDs and CdS nanoparticles. Fig. 1e shows the high angle annular dark field-scanning transmission electron microscopy (HAADF-STEM) image and corresponding EDX mapping of the sample CG1.0, in which the signals for Cd, S, and C elements are all uniformly present in the sample, confirming that the nanohybrids consist of CdS and GQDs. Such a structural feature suggests the effective coupling of CdS to GQDs, which may impart resulting nanohybrids with an intimate contact, which is crucial to achieving a promoted interfacial charge transfer.

Fig. 1f shows the XRD patterns of the samples. The pure CdS nanoparticles (sample CG0) are well-crystallized in hexagonal crystal phase as a result of hydrothermal treatment, and all the CdS/GQDs samples exhibit the similar XRD patterns to sample CG0, suggesting that the existence of GQDs could hardly affect the crystalline structure of CdS nanoparticles [31]. No characteristic diffraction peaks for GQDs could be detectable because of the low amount and/or high dispersion and relatively low diffraction intensity of GQDs [32]. The broad diffraction peaks reveal that crystallite sizes of CdS nanoparticles in the samples are relatively small. The crystallite sizes of the samples were calculated using Scherrer formula for the (111) facet diffraction peak, as listed in Table 1. Compared to sample CG0 (∼19.5 nm), the average crystallite size of CdS nanoparticles in nanohybrids is slightly increased to ∼20–24 nm depending on the GQD content. Thus, it can be inferred that the interaction between GQDs and CdS have an impact on the crystallization behaviors of CdS nanoparticles to a certain extent during hydrothermal coupling reactions. Note that our synthesis

Table 1
Effects of GQDs content on physicochemical properties and rate of H_2 evolution of CdS/GQDs nanohybrids.

Samples	S_{BET} ($m^2 g^{-1}$)[a]	Average pore size (nm)[b]	Total pore volume ($cm^3 g^{-1}$)[c]	Crystallite size (nm)[d]	H_2 evolution rate ($\mu mol\ h^{-1}$)
CG0	61.4	13.9	0.213	19.5	35.1
CG0.25	38.9	19.2	0.187	21.8	58.1
CG0.5	47.9	22.0	0.264	20.0	69.7
CG1.0	42.6	19.6	0.209	22.5	95.4
CG1.5	43.9	17.4	0.191	23.7	91.9
CG2.0	40.4	17.8	0.179	22.7	78.7
CG3.0	26.0	24.7	0.161	22.2	77.3

[a] BET surface area is calculated from the linear part of the BET plot.
[b] Adsorption average pore width (4 V/A by BET).
[c] Single point total pore volume of the pores at $P/P_0 = 0.99$.
[d] Average crystallite size is determined by the broadening of the CdS (111) facet diffraction peak using the Scherrer formula.

for nanohybrids started with low-crystallized cubic CdS nanoparticles and as-prepared GQDs, the crystallization of CdS nanoparticles and the coupling of GQDs and CdS could take place simultaneously under hydrothermal conditions.

The existence of GQDs in the CdS/GQDs and the chemical interaction between the two components was further characterized by FTIR, Raman and XPS. Fig. 2a shows the FT-IR spectra of the samples. The characteristic peaks of GQDs were observed at 3346 cm^{-1} for O—H vibration, 3207 and 1628 cm^{-1} for N—H vibration, 1558 cm^{-1} for C=C vibration, 1238 cm^{-1} for C—OH vibration, and 1077 cm^{-1} for C—O vibration [27,32,52]. As to the sample CG1.0, apart from the characteristic IR vibration peaks of CdS, several characteristic vibration peaks of GQDs occur, indicating the presence of GQDs. The existence of GQDs was further verified by Raman spectroscopy, as shown in Fig. 2b. In the Raman spectrum of pure CdS (sample CG0), two characteristic peaks at 294 and 597 cm^{-1} stemmed from the 1LO and 2LO vibration modes of hexagonal CdS, respectively [53]. For the sample CG1.0, besides the typical vibration peaks of CdS, there are two additional peaks at 1372 and 1584 cm^{-1}, which respectively correspond to the G and D bands of GQDs [32,52], further confirming the incorporation of GQDs. The chemical compositions of CdS/GQDs nanohybrids and the interaction between the two components are also studied by XPS analysis. As shown in Fig. 2c, the survey XPS spectrum of CG1.0 sample shows strong signals of Cd3d, S2p, C1 s and O 1s. The Cd 3d and S 2p signals come from CdS and the presence of C 1 s and O 1 s signals again confirms the existence of GQDs in the nanohybrids. The binding energies of Cd 3d and S 2p in their high-resolution XPS spectra (Fig. 2d and e) reveal that the chemical compositions of CdS is unchanged significantly in nanohybrids after coupling with GQDs under hydrothermal conditions. The C1 s XPS spectrum can be fitted by three main peaks at 284.7, 285.8, 286.7, and 288.5 eV, which can be attributed to the C=C, C—N, C—O, and C=O groups [32,52], respectively. These XPS results reveal that the GQDs were functionalized with oxygen-containing groups probably on edge sites, which can facilitate the coupling of GQDs with CdS nanocrystals by part of the oxygen-containing groups of GQDs binding to the CdS surface through the chemical linkages. As compared to pure CdS (sample CG0), the signals of Cd3d and S2p for sample CG1.0 are slightly shifted to higher binding energies (Fig. S4), implying the effective coupling of GQDs and CdS though a strong chemical interaction [32].

The effect of GQDs on the Brunauer-Emmett-Teller (BET) specific surface area (S_{BET}), pore size distribution, and pore structure of the resulting CdS/GQDs nanohybrids was studied using N_2 adsorption-desorption measurements at 77 K, as shown in Fig. 3a, Fig. S5, and Table 1. Clearly, the isotherm of pure CdS nanoparticles (sample CG0) can be classified into type IV isotherm with type H3 hysteresis loop, indicative of the presence of mesoporous structure in the samples, which are probably formed by the aggregations of primary CdS crystallites of ~20 nm. For the CdS/GQDs samples, it is

found that the decoration of GQDs on the surface of CdS has negligible effect on their nitrogen adsorption-desorption isotherms and pore size distribution curve. However, in comparison to the pure CdS (61.4 $m^2 g^{-1}$), all the CdS/GQDs nanohybrids show smaller S_{BET} and pore volume, which increase first and decrease afterwards with the increase in GQDs content, indicating that the presence of GQDs (~3 nm) may partially block surface mesopores of the aggregated CdS nanoparticles [54], forming a "dot-on-particle" structure. Notably, it is observed that the average pore size of CdS/GQDs nanohybrids shows a variation trend reversed to S_{BET} and pore volume, suggesting that the interparticle space can be expanded due to the coupling of GQDs on CdS surface, consistent with the TEM observations.

Fig. 3b shows the UV–vis diffuse reflectance spectra of pure CdS (sample CG0) and CdS/GQDs nanohybrids. All the CdS/GQDs nanohybrids exhibit similar intrinsic band gap absorption at ~560 nm (corresponding to a band gap of 2.2 eV) to pure CdS nanoparticles. This result reveals that the coupling of GQDs has no effect on the intrinsic optical properties of CdS and the GQDs exist on the surface of CdS nanoparticles instead of doping into the CdS. However, enhanced visible-light absorption is observed for the CdS/GQDs nanohybrids ranging from 560 to 800 nm relative to pure CdS, which is also reflected by their color change from yellow to dark yellow due to the absorption of GQDs (Fig. S6). Although the existence of GQDs endows additional visible light absorption at longer wavelength to nanohybrids, these absorbed photons could not be directly used to excite CdS/GQDs nanohybrids to generate more electrons and holes for promoting photocatalytic H_2 evolution reaction, which will be discussed in detail later.

The photocatalytic H_2 evolution activities of the samples were evaluated under visible light irradiation using 0.5 M Na_2S and 0.5 M Na_2SO_3 as the sacrificial reagents. Fig. 4a and Table 1 shows the average rates of H_2 evolution on different samples. The pure CdS nanoparticles (sample CG0) exhibit a low activity for H_2 evolution with a rate of 35.1 $\mu mol\ h^{-1}$ as expected due to the rapid recombination of photogenerated electrons and holes [55,56]. With the coupling a small amount of GQDs (0.25%) to CdS, the H_2 evolution rate of sample CG0.25 was enhanced to 58.1 $\mu mol\ h^{-1}$, and as the GQDs content increases further, the activity of CdS/GQDs nanohybrids gradually enhances and maximizes at 1.0% (CG1.0). The sample CG1.0 exhibits the highest H_2 evaluation rate of 95.4 $\mu mol\ h^{-1}$, which is 2.7 times higher than that of GC0. The AQE of CG1.0 is determined to be 4.2% under the light irradiation of 420 nm. Further increase in GQDs content will lead to a decrease in H_2 evaluation activity but these samples (CG1.5, CG2.0, and CG3.0) are still more active than CG0. In sharp contrast, the control experiments show that the GQDs alone have no activity for H_2 evaluation reactions. CdS nanoparticles physically mixed with GQDs with an exact same GQDs content as sample CG1.0 also show photocatalytic performance inferior to that of CG1.0, showing the importance of chemical interaction between two components for
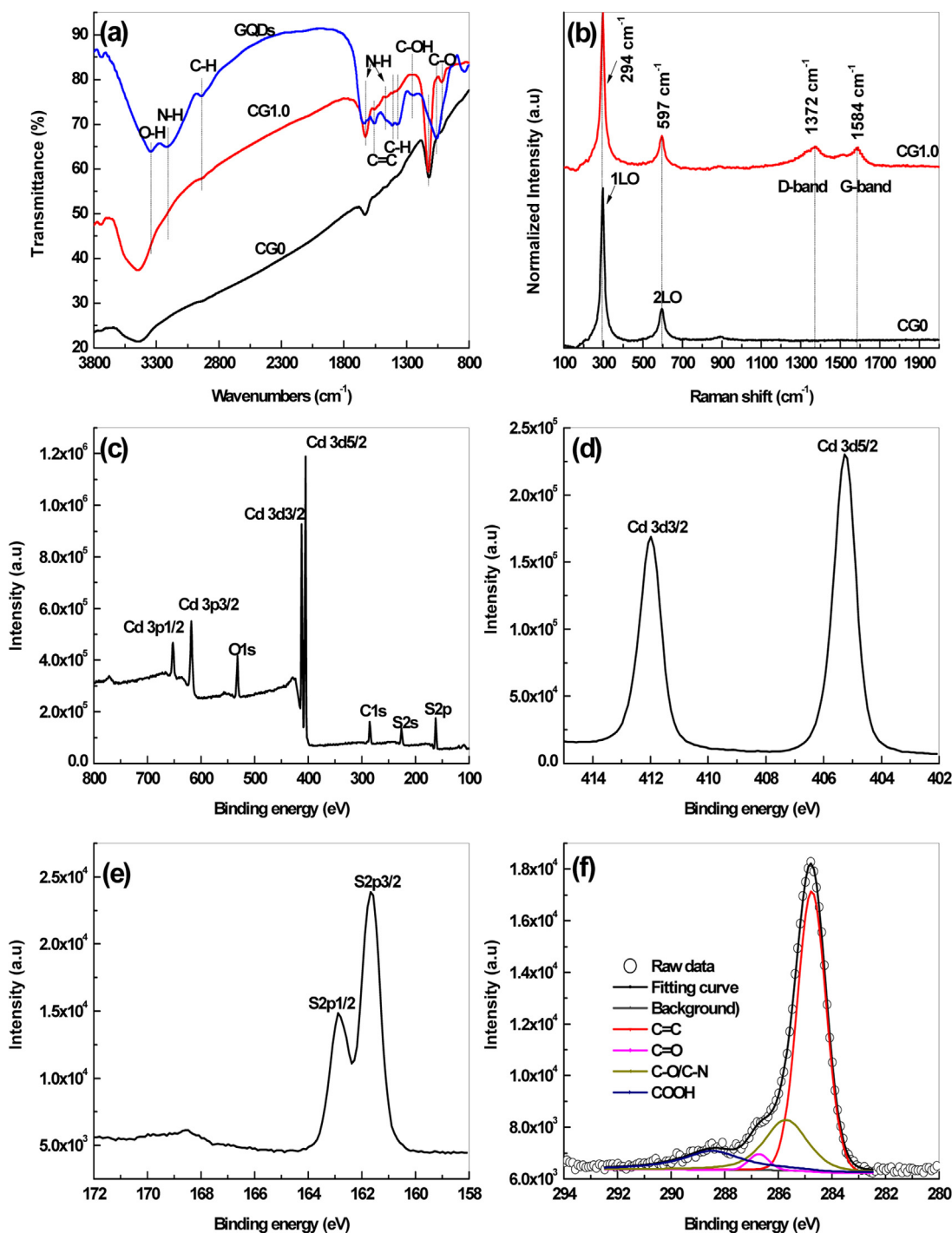
Fig. 2. (a) FT-IR spectra of GQDs, pure CdS (CG0 sample), and CG1.0 nanohybrid. (b) Raman spectra of pure CdS (sample CG0) and CG1.0 nanohybrid. (c) XPS survey spectrum of CG1.0 nanohybrid and high-resolution XPS spectra of (d) Cd 3, (e) S 2p, and (f) C1s core levels for CG1.0 nanohybrid.

enhance activity. Moreover, the photocatalytic stability of samples CG0 and CG1.0 was evaluated by carrying out a 36 h H_2 evolution experiment, with intermittent evacuation every 12 h, as show in Fig. 4b. Although the photocatalytic H_2 evolution activities of both CG1.0 and CG0 slowly decreased with prolonged reaction time, the CG1.0 still exhibits higher activity than CG0 after third-run reaction. The decrease in activity for CG0 is probably a result of photocorrosion due to the inefficient consumption of photogenerated holes by sacrificial reagent. As to the CG1.0 sample, apart from photocorrosion, the chemical interaction between CdS and GQDs would

be weaken during the long-term H_2 evolution process due to the photoxidative reactions, which is also proposed to be a main reason.

Above results clearly show that the incorporation of GQDs is effective to enhance the photocatalytic activity of CdS for H_2 evolution, and thus the essential roles of GQDs need to be clearly revealed. It has been previously proposed that the GQDs may act as a photosensitizer for improving light utilization and an electron acceptor for promoting the charge separation efficiency, as a result, the photocatalytic performance of the resulting SCs/GQDs materials can be greatly enhanced [23–36]. Note that our CdS/GQDs
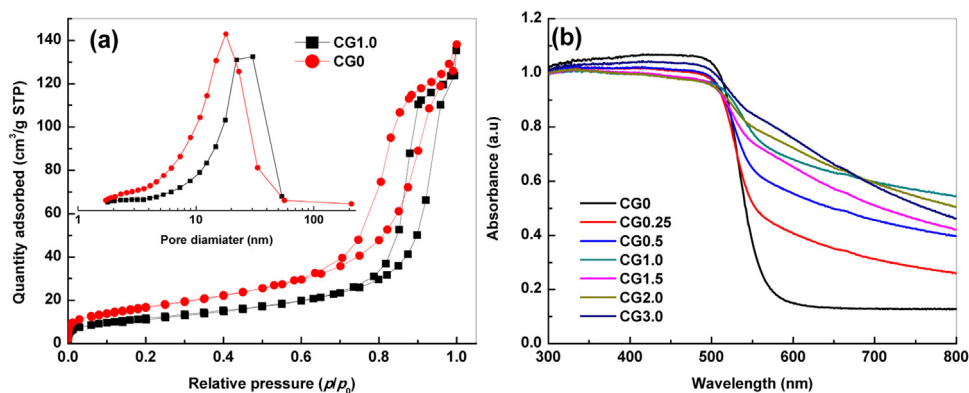
Fig. 3. (a) N$_2$ adsorption isotherms and the corresponding pore size distribution (inset) for pure CdS (sample CG0) and the CG1.0 nanohybrid. (b) UV–vis diffuse reflectance spectra of pure CdS (sample CG0) and CdS/GQDs nanohybrids.

nanohybrids show the extended visible light absorption ability (Fig. 3b), thus it is reasonable to expect that the photosensitization of GQDs could be responsible for the observed enhanced activity on CdS/GQDs nanohybrids, however, it is not the case in the present study. In order to clearly clarify this point, the excitation wavelength-dependent H$_2$ evolution activity was evaluated. The incident visible light with different wavelengths was obtained by employing various cut-off optical filters in front of light sources. Fig. 4c shows the time courses of H$_2$ evolution over CdS/GQDs nanohybrid (sample CG1.0). The same experiments were also carried out for pure CdS (sample CG0) and the time course of H$_2$ evolution was illustrated in Fig. S7. It is obvious that the CG1.0 can efficiently and steadily catalyze H$_2$ evolution under the light irra-

diation with shorter cut-off wavelengths such as 420 and 470 nm. When the cut-off wavelength of incident light increases further, the H$_2$ evolution activity decreases sharply, and there is almost no H$_2$ evolution as the wavelength reaches the absorption edge of the sample CG1.0. Similar results were also obtained for pure CdS (sample CG0) but with much lower H$_2$ activity as compared to CG1.0. Fig. 4d presents the average H$_2$ evolution rate within 12 h irradiation over CG0 and CG1.0 samples together with the UV–vis absorption spectrum of CG1.0, where the H$_2$ evolution rate of CG1.0 deviates from its light absorption spectrum especially at longer wavelengths and the photocatalytic activity of H$_2$ evolution along with wavelength coincided well with the UV–vis absorption spectrum of pure CdS, not that of CG1.0. These results clearly
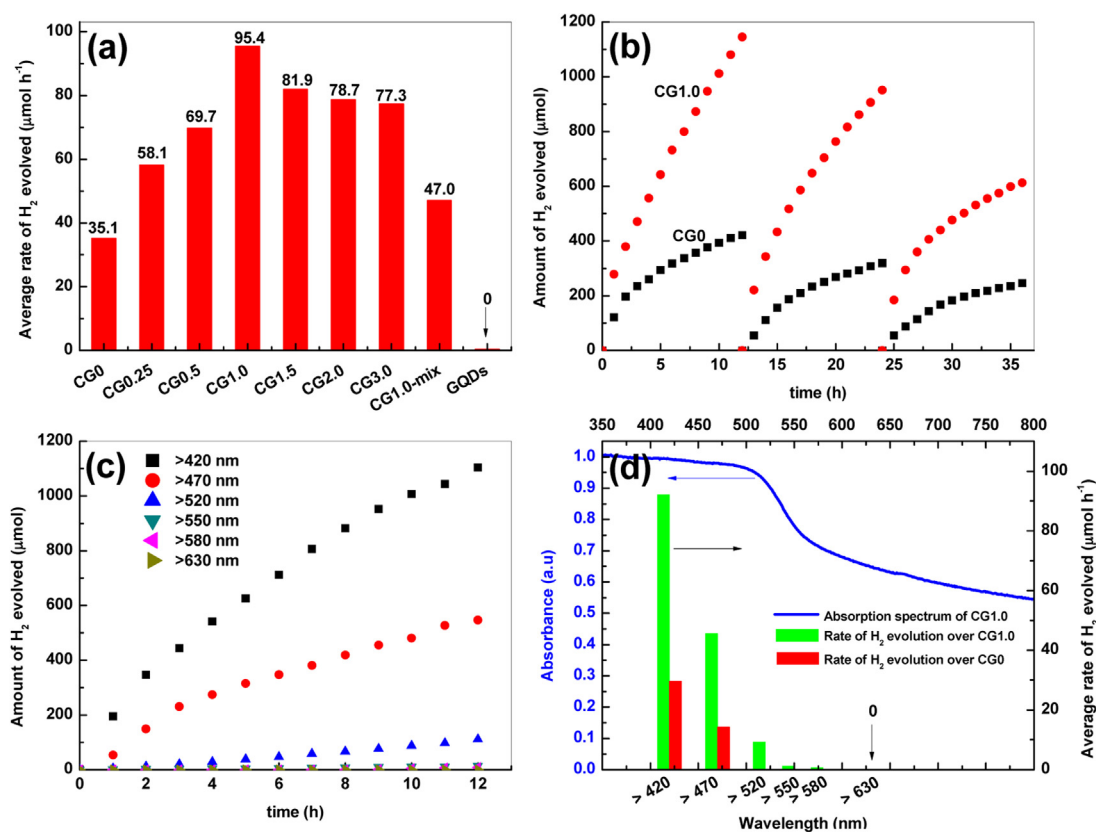
Fig. 4. (a) Average photocatalytic H$_2$ evolution rate over different samples. (b) Cycling test of photocatalytic H$_2$ evolution for pure CdS (CG0 sample) and CG1.0 nanohybrid. (c) Time courses of photocatalytic H$_2$ evolution activity of CG1.0 under the irradiation of different excitation wavelengths. (d) Wavelength-dependent average H$_2$ evolution rates over CG0 and CG1.0 together with the UV-vis-DRS spectrum of CG1.0 sample. Reaction conditions: 300W Xe lamp, $\lambda \geq 420$ nm; catalysts: 40 mg; 0.5 M Na$_2$S+ 0.5 M Na$_2$SO$_3$, 100 mL.
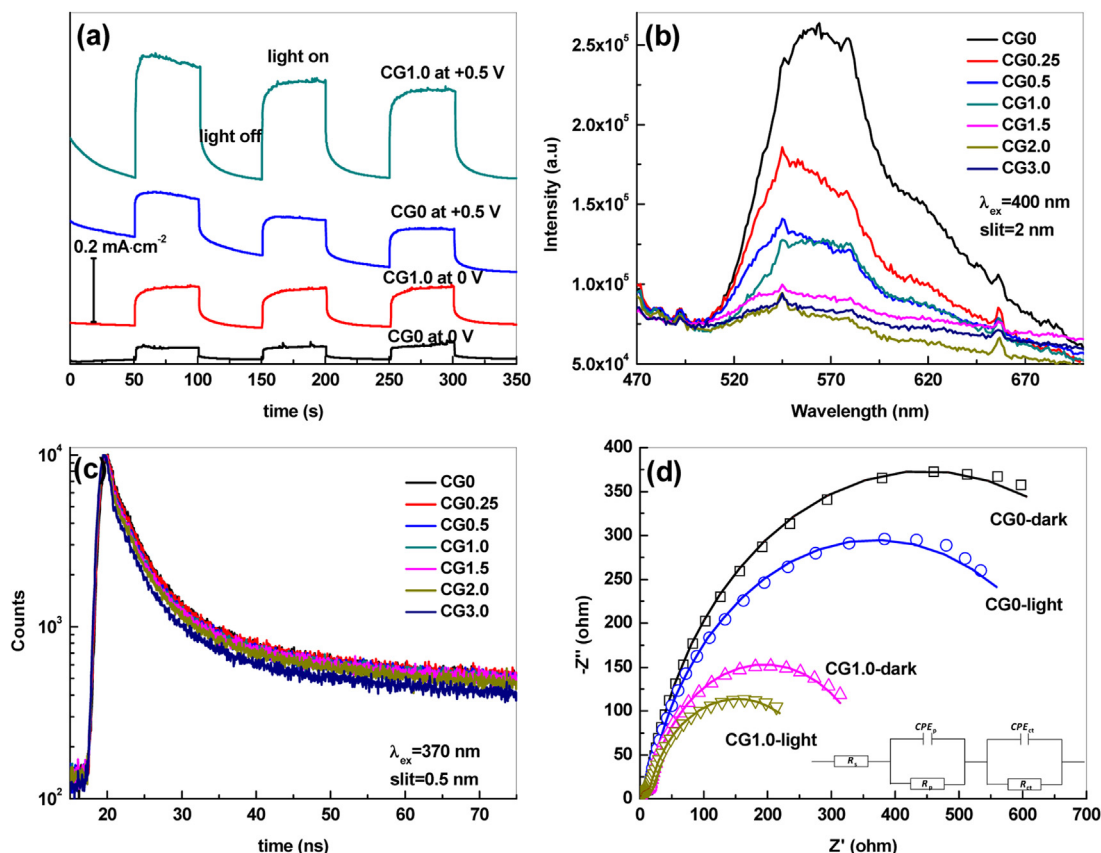
Fig. 5. (a) Transient photocurrent-time curves in 0.5 M Na_2SO_3/Na_2S aqueous solution at zero and 0.5 V forward biases under visible light irradiation. (b) Steady-state PL spectra of pure CdS and CdS/GQDs nanohybrids. Excitation wavelength is 400 nm with slit of 2 nm. (c) Time-resolved PL emission decay curves of pure CdS and CdS/GQDs nanohybrids. Excitation and detection wavelengths are 370 and 554 nm, respectively. (d) Electrochemical impendence curves of samples CG0 and CG1.0 recorded in 0.5 M Na_2SO_3/Na_2S aqueous solution in dark conditions and under visible light irradiation. The inset is equivalent circuit for simulating EIS curves.

demonstrate that the light absorption property of CdS in CdS/GQDs nanohybrids governs the reaction rate and the excess light absorption driven from GQDs has no contribution to the observed activity, suggesting that the GQDs may play a role of cocatalyst rather than a photosensitizer in this nanohybrid photocatalyst.

Considering that the GQDs contains graphene microdomains that may serve as an electron acceptor [2,3], and thus the electrons in the valence band (VB) of CdS could transfer to GQDs in the CdS/GQDs nanohybrids under light irradiation and lead to an efficient separation of photogenerated electrons and holes, which in turn results in enhanced photocatalytic performances. To confirm this hypothesis, the transient photocurrent responses of the sample CG1.0 were recorded under visible light irradiation. As shown in Fig. 5a, the presence of GQDs greatly enhances the photocurrent intensity of the CG1.0 sample relative to CG0 sample at both zero and 0.5 V forward biases, indicating that photogenerated electrons transfers more efficiently in the presence of GQDs, which is also supported by the evidence provided with steady-state and time-resolved PL results. As shown in Fig. 5b, all the CdS/GQDs nanohybrids display a remarkably reduced PL emission with the quenching efficiency of PL emission increases with the increase of GQDs content. The time-resolved PL decay spectra in Fig. 5c reveal that the emission decays for CdS/GQDs nanohybrids are faster than that of CG0 [28,32]. The PL results suggest that the coupling of GQDs to surface of CdS provides a rapid electron transfer pathway, hence greatly retarding the charge recombination of CdS. Furthermore, the dynamics for interfacial electron transfer were studied by electrochemical impedance spectroscopy (EIS). The AC impendence curves (Fig. 5d) of CG0 and CG1.0 electrodes were recorded in dark and under visible light irradiation at open circuit voltage

with the frequency varying from 100 kHz to 0.01 Hz. From Fig. 5d, a small single semicircle at the high frequency region and a larger semicircle at the low frequency region could be observed, from which the pore resistance (R_p) and charge-transfer resistance (R_{ct}) were determined by employing an equivalent circuit as shown in the inset of Fig. 5d and the data is listed in Table 2. The presence of R_p indicates that there is a hierarchical pore structures in the samples and the much smaller R_{ct} values for CG1.0 as compared to that of CG0 in dark and under light irradiation indicate that CQDs lead to a much lower charge transport resistance and much higher separation efficiency of electrons and holes [29,54]. Furthermore, the Mott-Schottky plots for the CG0 and CG1.0 electrodes were measured at a frequency of 1 kHz (Fig. S8), and the flat band potential (E_{fb}) and the majority-charge-carrier concentration (N_d) of the studied electrodes using the Mott-Schottky equation as follows:

$$\frac{1}{C^2} = \frac{2}{\varepsilon\varepsilon_0 qA^2 N_d}(E - E_{fb} - \frac{k_B T}{q})$$

where C is the interfacial capacitance, E is the applied potential, the constant A is the area, ε is the dielectric constant of the semiconductor, ε_0 is the permittivity of vacuum, T is the absolute temperature, q is the electronic charge, and k_B is the Boltzmann constant. The E_{fb} was determined to be −1.03 V for CG0 and −1.09 V for CG1.0, respectively, which are still more negative than the H^+/H_2 redox potential. Although the upward E_{fb} shift for CG1.0 is small but it still can help reducing the charge recombination and renders a higher reductive ability for reduction of H^+ to H_2. Moreover, the N_d of the CG1.0 sample was higher than that of CG0, indicating an effective separation of electrons and holes.

Table 2
Parameters evaluated for CG0 andCG1.0 electrodes through AC impedance measurements.

sample	E_{fb} (V *vs.* SCE)	N_d (cm^{-3})	Dark		Light	
			R_p (Ω)	R_{ct} (Ω)	R_p (Ω)	R_{ct} (Ω)
CG0	−1.03	1.17×10^{23}	11.98	871.80	11.70	713.60
CG1.0	−1.09	1.42×10^{23}	13.36	361.50	12.96	277.60
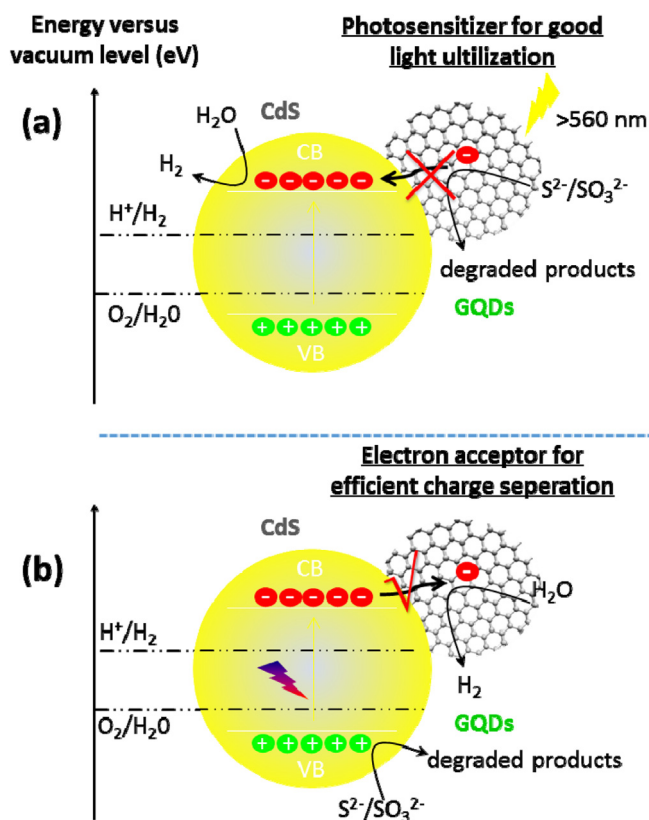
Scheme 2. Photocatalytic mechanism for enhanced hydrogen evolution activity over CdS/GQDs nanohybrids.

Based on above characterization results, a plausible photocatalytic mechanism for enhanced photocatalytic H$_2$ evolution activity on CdS/GQDs nanohybrids was proposed and illustrated in Scheme 2. GQDs are a derivate of graphene having smaller size with strong quantum effects and can be used as an organic semiconductor with good light absorption in visible region. It has been reported that GQDs itself showed photocatalytic activity for H$_2$ evolution under visible light irradiation (420 nm < λ < 800 nm), but the activity is extremely low albeit with high GQDs loading [20,21]. Inspired by this result, the GQDs were then used as a photosensitizer to improve the light utilization efficiency of semiconductors and enhanced PEC performances were observed under visible light with longer wavelengths, and there are only few examples showing enhanced performance for dye degradation [23] and H$_2$ evolution reactions [32]. However, our results show that although the GQDs can extend the light absorption of CdS, the CdS/GQDs nanohybrids hardly exhibit photocatalytic activity for H$_2$ evolution as the wavelength of incident light (>560 nm) beyond the band edge of the CdS. These results clearly indicate that the long-wavelength photons absorbed by nanohybrids due to the "black-box" effect of GQDs could not be used to produce excess electrons to induce a H$_2$ evolution reaction (Scheme 2a). However, it should be noted that when the wavelength (<560 nm) of the incident light, especially the light near to the UV region, matches with the HOMO-LUMO absorption region of GQDs, the possibility to improve the activity by absorbing additional photons derived from GQDs cannot be completely excluded. On the other hand, from the results of Fig. 5, the GQDs exhibits a graphene-like electronic properties, that is, it can serve as an electron acceptor to enhance the charge separation efficiency of the CdS/GQDs nanohybrids. Thermodynamically, it is reported that reported LUMO energy level of GQDs (−3.55 to −3.09 eV *vs.* vacuum energy level depending on size, functional groups, and edge sturctures, *etc.* [28,36,39,57]) is slightly less negative than that of CdS (−3.65 eV *vs.* vacuum energy level calculated based on the determined E_{fb}), thus the electrons most likely transfer from the CB of CdS to GQDs upon the light irradiation due to the small energy barrier at the intact interfaces. Also, the graphene microdomains in GQDs would provide a rapid electron transfer pathway due to its graphene-like conducting properties, thereby rendering an efficient electron-hole separation could be achieved, and hence enhancing the photocatalytic H$_2$ evolution activity of CdS/GQDs nanohybrids, as shown in Scheme 2b.

4. Conclusions

In summary, we have facilely developed strongly coupled CdS/GQDs nanohybrids as visible-light-driven photocatalysts for remarkable photocatalytic H$_2$ evolution reactions. The GQDs were uniformly and strongly decorated on CdS nanoparticles through a hydrothermal method, forming a "dot-on-particle" structure, and the amount of GQDs could be easily controlled. XPS and UV-vis-DRS results indicated that there is a strong interaction between the two components, and the presence of GQDs greatly extended the light absorption of nanohybrids beyond the band edge of CdS. Under the visible light irradiation (≥420 nm), the resulting CdS/GQDs nanohybrids exhibited a significantly higher photocatalytic H$_2$ activity and long-term reaction stability (36 h) than that of pure CdS photocatalyst. The H$_2$ evolution rate for CdS/GQDs nanohybrid with a GQDs content of 1.0% (sample CG1.0) was 2.7 times higher that of pure CdS sample. The AQE of photocatalytic H$_2$ evolution reached 4.2% at 420 nm. Moreover, the results of excitation-wavelength dependent experiments indicated that the light absorption of CdS in CdS/GQDs nanohybrids mainly governed the reaction rate and the excess light absorption derived from GQDs has no contribution to the observed high activity. The results of photocurrent response, steady-state and time-resolved PL, and EIS measurements revealed that the photocatalytic activity enhancement of CdS/GQDs could be attributed to the graphene-like feature of GQDs, which can provide a rapid electron transfer pathway to achieve efficient charge separation, and hence improving photocatalytic H$_2$ evolution activity of CdS/GQDs nanohybrids. Our study clearly pointed out that the GQDs mainly played an essential role as electron acceptor instead of a photosensitizer in enhancing the photocatalytic performances of CdS/GQDs nanohybrids, which will provide a new insight into development of nanohybrids based on semiconductors and GQDs for efficient solar energy conversion photocatalysts and devices.

Appendix A. Supplementary data

Supplementary data associated with this article can be found, in the online version, at http://dx.doi.org/10.1016/j.apcatb.2017.05.063.

References

[1] L.S. Li, X. Yan, Colloidal graphene quantum dots, J. Phys. Chem. Lett. 1 (2010) 2572–2576.

[2] M. Bacon, S.J. Bradley, T. Nann, Graphene quantum dots, Part. Part. Syst. Charact. 31 (2014) 415–428.

[3] Z. Zhang, J. Zhang, N. Chen, L. Qu, Graphene quantum dots: an emerging material for energy-related applications and beyond, Energy Environ. Sci. 5 (2012) 8869–8890.

[4] L.B. Tang, R.B. Ji, X.M. Li, K.S. Teng, S.P. Lau, Size-dependent structural and optical characteristics of glucose-derived graphene quantum dots, Part. Part. Syst. Charact. 30 (2013) 523–531.

[5] S. Kim, S.W. Hwang, M.-K. Kim, D.Y. Shin, D.H. Shin, C.O. Kim, S.B. Yang, J.H. Park, E. Hwang, S.-H. Choi, G. Ko, S. Sim, C. Sone, H.J. Choi, S. Bae, B.H. Hong, Anomalous behaviors of visible luminescence from graphene quantum dots: interplay between size and shape, ACS Nano 6 (2012) 8203–8208.

[6] S.N. Baker, G.A. Baker, Luminescent carbon nanodots: emergent nanolights, Angew. Chem. Int. Ed. 49 (2010) 6726–6744.

[7] J. Peng, W. Gao, B.K. Gupta, Z. Liu, R. Romero-Aburto, L.H. Ge, L. Song, L.B. Alemany, X.B. Zhan, G.H. Gao, S.A. Vithayathil, B.A. Kaipparettu, A.A. Marti, T. Hayashi, J.J. Zhu, P.M. Ajayan, Graphene quantum dots derived from carbon fibers, Nano Lett. 12 (2012) 844–849.

[8] S.J. Zhu, J.H. Zhang, C.Y. Qiao, S.J. Tang, Y.F. Li, W.J. Yuan, B. Li, L. Tian, F. Liu, R. Hu, H.N. Gao, H.T. Wei, H. Zhang, H.C. Sun, B. Yang, Strongly green-photoluminescent graphene quantum dots for bioimaging applications, Chem. Commun. 47 (2011) 6858–6860.

[9] S.J. Zhu, Q.N. Meng, L. Wang, J.H. Zhang, Y.B. Song, H. Jin, K. Zhang, H.C. Sun, H.Y. Wang, B. Yang, Highly photoluminescent carbon dots for multicolor patterning, sensors, and bioimaging, Angew. Chem. Int. Ed. 52 (2013) 3953–3957.

[10] S.J. Zhu, J.H. Zhang, S.J. Tang, C.Y. Qiao, L. Wang, H.Y. Wang, X. Liu, B. Li, Y.F. Li, W.L. Yu, X.F. Wang, H.C. Sun, B. Yang, Surface chemistry routes to modulate the photoluminescence of graphene quantum dots: from fluorescence mechanism to up-conversion bioimaging applications, Adv. Funct. Mater. 22 (2012) 4732–4740.

[11] J. Zhao, G.F. Chen, L. Zhu, G.X. Li, Graphene quantum dots-based platform for the fabrication of electrochemical biosensors, Electrochem. Commun. 13 (2011) 31–33.

[12] J. Ju, W. Chen, D.-H. Kim, K.-H. Lim, J. Li, P. Chen, Synthesis of highly fluorescent nitrogen-doped graphene quantum dots for sensitive, label-free detection of Fe(III) in aqueous media, Biosens. Bioelectron. 58 (2014) 219–225.

[13] J.C. Ge, M.H. Lan, B.J. Zhou, W.M. Liu, L. Guo, H. Wang, Q.Y. Jia, G.L. Niu, X. Huang, H.Y. Zhou, X.M. Meng, P.F. Wang, C.-S. Lee, W.J. Zhang, X.D. Han, A graphene quantum dot photodynamic therapy agent with high singlet oxygen generation, Nat. Commun. 5 (2014) 4596–4604.

[14] B.Z. Ristic, M.M. Milenkovic, I.R. Dakic, B.M. Todorovic-Markovic, M.S. Milosavljevic, M.D. Budimir, V.G. Paunovic, M.D. Dramicanin, Z.M. Markovic, Vladimir S. Trajkovic, Photodynamic antibacterial effect of graphene quantum dots, Biomaterials 35 (2014) 4428–4435.

[15] Q.Q. Li, S. Zhang, L.M. Dai, L.-S. Li, Nitrogen-doped colloidal graphene quantum dots and their Size-dependent electrocatalytic activity for the oxygen reduction reaction, J. Am. Chem. Soc. 134 (2012) 18932–18935.

[16] Y. Li, Y. Zhao, H.H. Cheng, Y. Hu, G.Q. Shi, L.M. Dai, L.T. Qu, Nitrogen-doped graphene quantum dots with oxygen-rich functional groups, J. Am. Chem. Soc. 134 (2012) 15–18.

[17] Y. Song, S.W. Chen, Graphene quantum-dot-supported platinum nanoparticles: defect-mediated electrocatalytic activity in oxygen reduction, ACS Appl. Mater. Interfaces 6 (2014) 14050–14060.

[18] J.H. Shen, Y.H. Zhu, X.L. Yang, C.Z. Li, Graphene quantum dots: emergent nanolights for bioimaging, sensors, catalysis and photovoltaic devices, Chem. Commun. 48 (2012) 3686–3699.

[19] D. Qu, M. Zheng, P. Du, Y. Zhou, L. Zhang, D. Li, H. Tan, Z. Zhao, Z. Xie, Z. Sun, Highly luminescent S, N co-doped graphene quantum dots with broad visible absorption bands for visible light photocatalysts, Nanoscale 5 (2013) 12272–12277.

[20] T.-F. Yeh, C.-Y. Teng, S.-J. Chen, H.S. Teng, Nitrogen-doped graphene oxide quantum dots as photocatalysts for overall water-splitting under visible light illumination, Adv. Mater. 26 (2014) 3297–3303.

[21] T.-F. Yeh, S.-J. Chen, H.S. Teng, Synergistic effect of oxygen and nitrogen functionalities for graphene-based quantum dots used in photocatalytic H_2 production from water decomposition, Nano Energy 12 (2015) 476–485.

[22] M. Roushani, M. Mavaei, H.R. Rajabi, Graphene quantum dots as novel and green nanomaterials for the visible-light-driven photocatalytic degradation of cationic dye, J. Mol. Catal. A: Chem. 409 (2015) 102–109.

[23] S.J. Zhuo, M.W. Shao, S.-T. Lee, Upconversion and downconversion fluorescent graphene quantum dots: ultrasonic preparation and photocatalysis, ACS Nano 6 (2012) 1059–1064.

[24] D. Pan, C. Xi, Z. Li, L. Wang, Z. Chen, B. Lu, M. Wu, Electrophoretic fabrication of highly robust efficient, and benign heterojunction photoelectrocatalysts based on graphene-quantum-dot sensitized TiO₂ nanotube arrays, J. Mater. Chem. A 1 (2013) 3551–3555.

[25] D.K.L. Chan, P.L. Cheung, J.C. Yu, A visible-light-driven composite photocatalyst of TiO₂ nanotube arrays and graphene quantum dots, Beilstein J. Nanotechnol. 5 (2014) 689–695.

[26] B.K. Gupta, G. Kedawat, Y. Agrawal, P. Kuma, J. Dwivedi, S.K. Dhawan, A novel strategy to enhance ultraviolet light driven photocatalysis from graphene quantum dots infilled TiO₂ nanotube arrays, RSC Adv. 5 (2015) 10623–10631.

[27] D.Y. Pan, J.K. Jiao, Z. Li, Y.T. Guo, C.Q. Feng, Y. Liu, L. Wang, M.H. Wu, Efficient separation of electron-hole pairs in graphene quantum dots by TiO₂ heterojunctions for dye degradation, ACS Sustain. Chem. Eng. 3 (2015) 2405–2413.

[28] K.-A. Tsai, Y.-J. Hsu, Graphene quantum dots mediated charge transfer of CdSe nanocrystals for enhancing photoelectrochemical hydrogen production, Appl. Catal. B: Environ. 164 (2015) 271–278.

[29] S. Yu, Y.-Q. Zhong, B.-Q. Yu, S.-Y. Cai, L.-Z. Wu, Y. Zhou, Graphene quantum dots to enhance the photocatalytic hydrogen evolution efficiency of anatase TiO₂ exposed with {001} facet, Phys. Chem. Chem. Phys. 18 (2016) 20338–20344.

[30] A.L. Qu, H.L. Xie, X.M. Xu, Y.Y. Zhang, S.W. Wen, Y.F. Cui, High quantum yield graphene quantum dots decorated TiO₂ nanotubes for enhancing photocatalytic activity, Appl. Surf. Sci. 375 (2016) 230–241.

[31] T. Fan, Y.L. Li, J.F. Shen, M.X. Ye, Novel GQD-PVP-CdS composite with enhanced visible-light-driven photocatalytic properties, Appl. Surf. Sci. 367 (2016) 518–527.

[32] S.X. Min, J.H. Hou, Y.G. Lei, X.H. Ma, G.X. Lu, Facile one-step hydrothermal synthesis toward strongly coupled TiO₂/graphene quantum dots photocatalysts for efficient hydrogen evolution, Appl. Surf. Sci. 396 (2017) 1375–1382.

[33] C.X. Guo, Y.Q. Dong, H.B. Yang, C.M. Li, Graphene quantum dots as a green sensitizer to functionalize ZnO nanowire arrays on F-Doped SnO₂ glass for enhanced photoelectrochemical water splitting, Adv. Energy Mater. 3 (2013) 997–1003.

[34] M. Dutta, S. Sarkar, T. Ghosh, D. Basak, ZnO/graphene quantum dot solid-state solar cell, J. Phys. Chem. C 116 (2012) 20127–20131.

[35] P. Gao, K. Ding, Y. Wang, K.Q. Ruan, S.L. Diao, Q. Zhang, B.Q. Sun, J.S. Jie, Crystalline Si/graphene quantum dots heterojunction solar cells, J. Phys. Chem. C 118 (2014) 5164–5171.

[36] Z.L. Zhu, J.N. Ma, Z.L. Wang, C. Mu, Z.T. Fan, L.L. Du, Y. Bai, L.Z. Fan, H. Yan, D.L. Phillips, S.H. Yang, Efficiency enhancement of perovskite solar cells through fast electron extraction: the role of graphene quantum dots, J. Am. Chem. Soc. 136 (2014) 3760–3763.

[37] X. Yan, X. Cui, B. Li, L.S. Li, Large, solution-processable graphene quantum dots as light absorbers for photovoltaics, Nano Lett. 10 (2010) 1869–1873.

[38] J.K. Kim, M.J. Park, S.J. Kim, D.H. Wang, S.P. Cho, S. Bae, J.H. Park, B.H. Hong, Balancing light absorptivity and carrier conductivity of graphene quantum dots for high-efficiency bulk heterojunction solar cells, ACS Nano 7 (2013) 7207–7212.

[39] Y. Li, Y. Hu, Y. Zhao, G.Q. Shi, L.E. Deng, Y.B. Hou, L.T. Qu, An electrochemical avenue to green-luminescent graphene quantum dots as potential electron-acceptors for photovoltaics, Adv. Mater. 23 (2011) 776–780.

[40] L.J. Chen, C.X. Guo, Q.M. Zhang, Y.L. Lei, J.L. Xie, S.J. Ee, G.H. Guai, Q.L. Song, C.M. Li, Graphene quantum-dot-doped polypyrrole counter electrode for high-performance dye-sensitized solar cells, ACS Appl. Mater. Interfaces 5 (2013) 2047–2052.

[41] E. Lee, J. Ryu, J. Jang, Fabrication of graphene quantum dots via size-selective precipitation and their application in upconversion-based DSSCs, Chem. Commun. 49 (2013) 9995–9997.

[42] X.L. Fang, M.Y. Li, K.M. Guo, J. Li, M.C. Pan, L.H. Bai, M.D. Luoshan, X.Z. Zhao, Graphene quantum dots optimization of dye-sensitized solar cells, Electrochim. Acta 137 (2014) 634–638.

[43] J. Huang, Y.J. Wu, D.D. Wang, Y.F. Ma, Z.K. Yue, Y.T. Lu, M.X. Zhang, Z.J. Zhang, P. Yang, Silicon phthalocyanine covalently functionalized N-doped ultrasmall reduced graphene oxide decorated with Pt nanoparticles for hydrogen evolution from water, ACS Appl. Mater. Interfaces 7 (2015) 3732–3741.

[44] P.J. Yang, J.H. Zhao, J. Wang, H.J. Cui, L. Li, Z.P. Zhu, Multifunctional nitrogen-doped carbon nanodots for photoluminescence, sensor, and visible-light-induced H_2 production, ChemPhysChem 16 (2015) 3058–3063.

[45] M. Mahyari, Y. Bide, J.N. Gavgani, Iron(III) porphyrin supported on S and N co-doped graphene quantum dot as an efficient photocatalyst for aerobic oxidation of alcohols under visible light irradiation, Appl. Catal. A: Gen. 517 (2016) 100–109.

[46] A. Kudo, Y. Miseki, Heterogeneous photocatalyst materials for waters plitting, Chem. Soc. Rev. 38 (2009) 253–278.

[47] A. Kudo, Recent progress in the development of visible light-driven powdered photocatalysts for water splitting, Int. J. Hydrogen Energy 32 (2007) 2673–2678.

[48] X.B. Chen, S.H. Shen, L.J. Guo, S.S. Mao, Semiconductor-based photocatalytic hydrogen generation, Chem. Rev. 110 (2010) 6503–6570.

[49] Q. Li, B.D. Guo, J.G. Yu, J.R. Ran, B.H. Zhang, H.J. Yan, J.R. Gong, Highly efficient visible-light-driven photocatalytic hydrogenproduction of CdS-cluster-decorated graphene nanosheets, J. Am. Chem. Soc. 133 (2011) 10878–10884.

[50] H. Li, Z.B. Xia, J.Q. Chen, L. Lei, J.H. Xing, Constructing ternary CdS/reduced graphene oxide/TiO_2 nanotube arrays hybrids for enhanced visible-light-driven photoelectrochemical and photocatalytic activity, Appl. Catal. B: Environ. 168–169 (2015) 105–113.

[51] Z.D. Meng, M.M. Peng, L. Zhu, W.-C. Oh, F.J. Zhang, Fullerene modification CdS/TiO_2 to enhancement surface area and modification of photocatalytic activity under visible light, Appl. Catal. B: Environ. 113–114 (2012) 141–149.

[52] L. Wang, Y. Wang, T. Xu, H. Liao, C. Yao, Y. Liu, Z. Li, Z. Chen, D. Pan, L. Sun, M. Wu, Gram-scale synthesis of single-crystalline graphene quantum dots with superior optical properties, Nat. Commun. 5 (2014) 5357–5366.

[53] R. Bera, S. Kundu, A. Patra, 2D hybrid nanostructure of reduced graphene oxide-CdS nanosheet for enhanced photocatalysis, ACS Appl. Mater. Interfaces 7 (2015) 13251–13259.

[54] Q. Li, C. Cui, H. Meng, J.G. Yu, Visible-light photocatalytic hydrogen production activity of $ZnIn_2S_4$ microspheres using carbon quantum dots and platinum as dual cocatalysts, Chem. Asian J. 9 (2014) 1766–1770.

[55] X. Zong, H.J. Yan, G.P. Wu, G.J. Ma, F.Y. Wen, L. Wang, C. Li, Enhancement of photocatalytic H_2 evolution on CdS by loading MoS_2 as cocatalyst under visible light irradiation, J. Am. Chem. Soc. 130 (2008) 7176–7177.

[56] A.P. Wu, C.G. Tian, Y.Q. Jiao, Q. Yan, G.Y. Yang, H.G. Fu, Sequential two-step hydrothermal growth of MoS_2/CdS core-shell heterojunctions for efficient visible light-driven photocatalytic H_2 evolution, Appl. Catal. B: Environ. 203 (2017) 955–963.

[57] V. Gupta, N. Chaudhary, R. Srivastava, S. Chand, Luminscent graphene quantum dots for organic photovoltaic devices, J. Am. Chem. Soc. 133 (2011) 9960–9963.